EES Catalysis

PAPER

View Article Online
View Journal | View Issue

Cite this: *EES Catal.*, 2025, 3, 566

Above 2 W cm^{-2} direct liquid fuel cells enabled by mitigating cathode polarization†

Yu Guo,[ab] Fukang Gui,[b] Yangkai Han,[cd] Yingjian Cao,[b] Zijun Hu,[b] Yongkang Han,[b] Qinggang Tan,[e] Yong Che,[f] Cunman Zhang,[b] Yun Zhao *[c] and Qiangfeng Xiao *[b]

Received 9th January 2025,
Accepted 12th March 2025

DOI: 10.1039/d5ey00005j

rsc.li/eescatalysis

Among direct liquid fuel cells, the direct borohydride fuel cells (DBFCs) are considered as attractive portable or mobile power sources due to their high theoretical voltage and high energy density. However, the development of DBFCs has been greatly hindered by the borohydride crossover and oxidation at the cathode. Here we have developed DBFCs featuring a borohydride-tolerant Mn–Co–C spinel cathode catalyst and a microscale bipolar interface constituting a poly(arylene piperidinium) anion exchange membrane and Nafion®-based cathode that can achieve breakthroughs in performance and scalability. The areal peak power density surpasses 2 W cm^{-2} at 80 °C with a platinum loading less than 1 mg cm^{-2}. The three-electrode and crossover studies elucidate that the cathode polarization is significantly mitigated by the suppressed parasitic borohydride oxidation as compared with conventional configurations. The success of transforming the performance from a single cell of 1.5 × 1.5 to 5 × 5 cm^2 paves the way for practical applications.

Broader context

In the broader context of energy and environmental science, developing clean energy technologies is of utmost importance. Proton exchange membrane fuel cells (PEMFCs) show great potential but face significant challenges, such as high catalyst and membrane costs, difficult hydrogen storage, and insufficient infrastructure. Direct liquid fuel cells, particularly direct borohydride fuel cells (DBFCs), present a promising solution to these challenges, offering high volumetric energy density and ease of refueling. However, the advancement of DBFCs has been significantly hindered by borohydride crossover and cathodic oxidation issues. In this work, we have developed DBFCs featuring a borohydride-tolerant Mn–Co–C spinel cathode catalyst and a microscale bipolar interface constituting a poly(arylene piperidinium) anion exchange membrane and Nafion®-based cathode, achieving breakthroughs in both performance and scalability.

Introduction

Fuel cells directly convert the free energy of the oxidation of fuels into electricity without the Carnot cycle limitation of a heat engine.[1] They have emerged as a promising source of low-emission power generation for transportation, stationary power systems and portable devices, transitioning our society from a traditional fossil-fuel-based economy to a renewable energy economy.[2] Although great progress has been achieved in the transportation sector, the widespread commercialization of polymer electrolyte membrane fuel cells (PEMFCs) is limited by the high material cost and lack of hydrogen infrastructure, such as the storage, transportation, and distribution.[3] Alternatively, extensive efforts have been devoted to developing direct liquid fuel cells (DLFCs) due to their attractive features such as high energy density, small fuel cartridges, and convenient storage and transportation.[4,5] As compared with the DLFCs with fuels such as methanol, ethanol, hydrazine, ammonia, formic acid, ethylene glycol, dimethyl ether *etc.*, the direct borohydride fuel cells (DBFCs) that operate with sodium borohydride as the fuel and oxygen as the oxidant are increasingly

[a] *Key Laboratory of Advanced Manufacturing Technology for Automobile Parts, Ministry of Education, Chongqing University of Technology, Chongqing, China*
[b] *School of Automotive Studies & Clean Energy Automotive Engineering Center, Tongji University (Jiading Campus), 4800 Cao'an Road, Shanghai 201804, China. E-mail: xiaoqf@tongji.edu.cn*
[c] *Fuel Cell System and Engineering Laboratory, Key Laboratory of Fuel Cells & Hybrid Power Sources, Dalian Institute of Chemical Physics, Chinese Academy of Sciences, Dalian, 116023, China. E-mail: yunzhao@dicp.ac.cn*
[d] *University of Chinese Academy of Sciences, Beijing, 100049, China*
[e] *School of Materials Science & Engineering, Tongji University (Jiading Campus), 4800 Cao'an Road, Shanghai, 201804, China*
[f] *Enpower Beijing Corp., 13 Area 2 Jinsheng Street, Daxing, Beijing, 102600, China*
† Electronic supplementary information (ESI) available. See DOI: https://doi.org/10.1039/d5ey00005j

gaining research interest from the scientific community due to high theoretical voltage (1.64 V) and high energy density (9.3 kW h kg^{-1}).[6,7] $NaBH_4$ is a water-soluble, environmentally safe, and carbon-neutral fuel, which can be converted into $NaBO_2$ by a complete 8-electron electrooxidation. $NaBO_2$ as an environmentally safe product can be regenerated into $NaBH_4$ by thermochemical or electrochemical methods,[8] which makes DBFCs a sustainable power source. Moreover, $NaBH_4$ manifests high stability in strongly alkaline aqueous solutions, making it possible to employ low-cost anion exchange membranes as electrolytes. However, DBFCs are still far from commercialization as they are limited by poor performance and high-cost catalysts.

Current efforts to improve DBFC performance comprise the development of catalysts and membranes, and the design of cell configurations. Numerous materials have been investigated as anode catalysts for the direct borohydride oxidation reaction (BOR), including Pt, Pd, Au, Ag, Ir, Rh, Ru, and their alloys as well as non-precious metals (*e.g.*, Ni and Cu), hydrogen storage alloys, metal borides, metal oxides, and metal phosphides.[9–12] Among these catalysts, Pt-based ones show high electroactivity towards the BOR and hydrogen oxidation, thus enabling high performance of DBFCs. However, their practical applications in DBFCs are hampered by the high cost and limited crustal abundance. Moreover, Pt-based catalysts are also widely used as cathode oxygen reduction reaction (ORR) catalysts, which further improve the noble metal loadings in DBFCs. Additionally, a detrimental mixed potential can be generated due to the crossover of borohydride.[13] Non-noble ORR catalysts, such as metal–nitrogen–carbon (*e.g.*, Fe–N–C and Co–N–C),[14] transitional metal oxides (*e.g.*, MnO_2, MnO_x/C, $NiMnO_x$/C)[15,16] and perovskites (*e.g.*, $LaNi_{0.8}Co_{0.2}O_3$ and $LaNiO_3$)[17] are considered to be promising candidates thanks to their high activity and good tolerance towards BH_4^- in alkaline environments. Both cation and anion exchange membranes have been adopted as electrolytes to separate the anode and cathode. The Nafion® membrane is the most extensively used cation exchange membrane in DBFCs since it can mitigate the BH_4^- crossover by the electrostatic repulsion between $-SO_3^{2-}$ anions from Nafion® side chains and BH_4^-.[18] As compared with Nafion®, anion exchange membranes have lower cost and well-balanced chemistry, yet are plagued with BH_4^- crossover.[10,19,20] Great efforts, including cross-linking,[21,22] alkali-doping,[23] compositing with carbon nanotubes,[24] and modification with BOR electrocatalysts,[25] have been made to develop various membranes for DBFCs. Besides the progress at the material level, the design of the electrode structure has been proven to be another important dimension for improving the fuel cell performance. When liquid H_2O_2 was chosen as the cathode oxidant, the bipolar interface configuration enabled the DBFCs to operate in sharply different local pH environments at the anode and cathode and deliver a high peak power density of 630 mW cm^{-2}.[26] Despite these strategies, the BH_4^- crossover and high cathode polarization still dramatically sacrifice the open circuit voltage (OCV) and output power density, and in turn, hamper the practical implementation of DBFCs.

Here we have developed high-performance DBFCs by mitigating cathode polarization through the combination of borohydride-tolerant Mn–Co–C spinel cathode catalysts and a microscale bipolar interface constituting a poly(arylene piperidinium) anion exchange membrane and Nafion®-based cathode. As illustrated in Fig. 1a, the conventional DBFCs are operated with a cation exchange membrane in Na^+ or K^+ form for NaOH or KOH-based anolytes, respectively, causing the cell Ohmic drop due to the low conductivity. Moreover, Na^+ or K^+ cations migrate from the anode to the cathode during operation, followed by combining with OH^- from the ORR and precipitating in the cathode pores. As a result, the reduced O_2 mass transport is unavoidable. Additionally, the conductivity and stability of anodes decrease due to the lowered alkaline concentration. All these factors contribute to the inferior performance of DBFCs.[18,27,28] In our configuration (Fig. 1b), the poly(arylene piperidinium) anion exchange membrane (Fig. S1a, ESI†) and cationic Nafion® ionomer in the cathode form a microscale bipolar interface which effectively reduces the oxidation of permeated BH_4^- on the cathode catalyst and in turn the cathode overpotential. The BH_4^--tolerant Mn–Co–C spinel cathode catalyst not only further mitigates the effect of the permeated BH_4^- but also decreases the cost of DBFCs.[29] The formed OH^- ions in the ORR migrate from the cathode to the anode through the poly(arylene piperidinium) anion exchange membrane and balance OH^- ions consumed in the BOR. In addition, the membrane is 15 μm and has an ionic conductivity of 140 mS cm^{-1} at 80 °C. The resultant DBFCs can deliver unprecedented areal peak power densities of 2.33 and 1.53 W cm^{-2} for Pt loadings of 0.75 and 0.15 mg cm^{-2} at 80 °C, respectively.

Results and discussion

Impact of the fuel cell configuration on DBFC performance

The membrane electrode assembly constitutes carbon cloth as an anode catalyst substrate, polymeric anion or cation exchange membrane, and carbon paper as the cathode catalyst substrate and gas diffusion layer. The typical structure for the Mn–Co–C spinel cathode is shown in Fig. 1c and d. The catalyst layer is quite uniform with a thickness of ~23.86 μm. Consistent with our previous work and reported literature,[29,30] there are perpendicular cracks formed within the catalyst layer. For the anode, the Pt/C catalyst is uniformly coated onto the carbon fibers of the braided carbon cloth as shown in Fig. 1e and f. To investigate the effect of the electrode/membrane interface on DBFC performance, five different types of DBFCs were constructed by a combinatorial approach. They are denoted as "anode ionomer/membrane/cathode ionomer", namely, A/A/A, A/A/C, C/A/A, C/A/C, and C/C/C, where A represents Alkymer®-based (poly(arylene piperidinium)) anion exchange ionomer or membrane (AEI or AEM) and C is a cation exchange ionomer (Nafion®) or membrane (Gore-select®) (CEI or CEM). The anode was made from a low-loading commercial Pt/C catalyst (40 wt% Pt on Vulcan XC-72 carbon support, 0.15 mg_{Pt} cm^{-2}) in

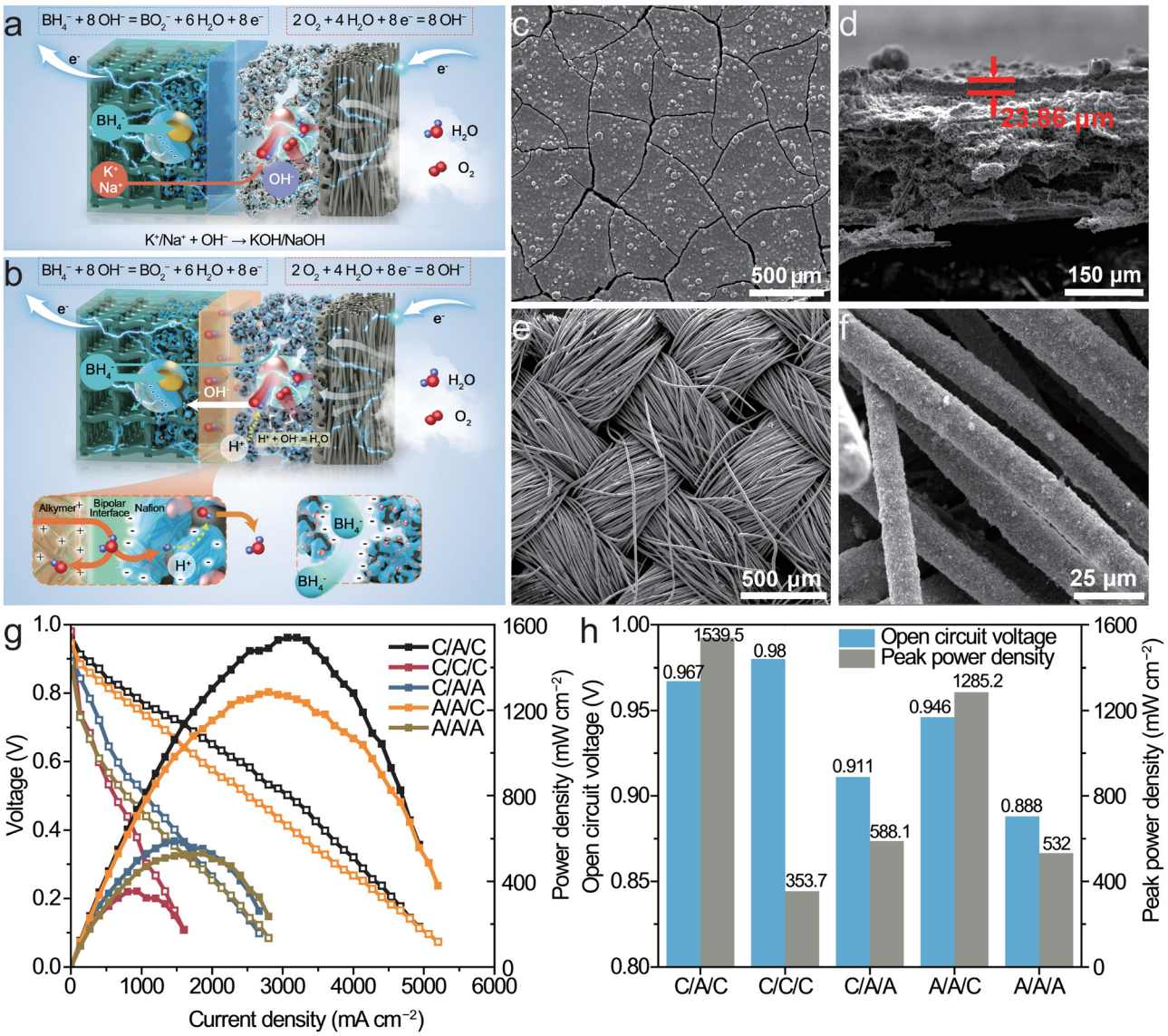

Fig. 1 DBFC configuration and electrochemical performance. (a) Schematics of conventional DBFC with cation exchange membrane as the electrolyte. (b) Schematics of DBFC using cathode microscale bipolar interface. (c) Top-view and (d) cross-sectional SEM images of the cathode with carbon paper as the catalyst substrate and gas diffusion layer. (e) Low and (f) high magnification SEM images of the anode with carbon cloth as the catalyst substrate. (g) *I*–*V* polarization and power density of DBFCs with different configurations. (h) Comparison of open circuit voltage and peak power density of DBFCs with different configurations.

light of its superior BOR activity. The Mn–Co-BP2000 spinel developed in our previous work was employed as a cathode catalyst with a loading of 1.5 mg cm^{-2}.[29] Fig. 1g shows the voltage polarizations and power densities as a function of current density measured under 80% humidified O_2 at a flow rate of 0.5 normal liter per minute (NLPM). The open cell voltage (OCV) is intimately related to the mixed potentials at the cathode caused by BH_4^- crossover and simultaneous oxidation of BH_4^- ions and hydrogen at the anode. When AEM is used as the electrolyte, the OCV increases from 0.888, 0.911, 0.946 to 0.967 V for A/A/A, C/A/A, A/A/C and C/A/C, respectively. It is seen that the cathode microscale bipolar interface (AEM/CEI) plays a critical role in improving the OCV. Consistent with the reported literature,[31] our observation (Movie S1 and S2, ESI†) shows much slower bubble evolution of anolyte in the presence of Pt/C anode with Nafion® ionomer than that with poly(arylene piperidinium)-based AEI, indicating that Nafion® can effectively mitigate the hydrolysis of BH_4^- to H_2 compared with AEI. As a result, the OCV can also increase when the anode ionomer changes from AEI to Nafion® because the theoretical OCV of DBFC (1.64 V) is higher than that of the H_2–O_2 fuel cell (1.23 V). As expected, the C/C/C configuration presents the highest OCV of 0.980 V due to the mitigated BH_4^- hydrolysis and limited crossover by the repulsion between BH_4^- and negatively-charged $-SO_3^{2-}$ side chains of CEM. The peak power density of C/C/C is 353.7 mW cm^{-2}, which is comparable to

those reported previously with Nafion® as the membrane in the literature and used as a basis for performance comparison between different DBFCs.[32–37] It was also found that the A/C/A, A/C/C and C/C/A configurations delivered even lower power density (Fig. S2–S4, ESI†) when CEM was used as the electrolyte. All the peak power densities are much lower than those for the DBFCs with AEM due to NaOH and KOH precipitation at the cathode. When the cathode microscale bipolar interface is used, the peak power density is greatly improved to 1285.2 mW cm^{-2} for A/A/C and 1539.5 mW cm^{-2} for C/A/C as compared with 532 mW cm^{-2} for A/A/A and 588.1 mW cm^{-2} for C/A/A. It is worth mentioning that both OCV and peak power density increase in the order of A/A/A < C/A/A < A/A/C < C/A/C when AEM is adopted in DBFCs. For better comparison, both peak power density and OCV are summarized in Fig. 1h. Obviously, the cathode microscale bipolar interface dominates the effect of improving the DBFC performance against the interface at the anode side.

Cathodic and anodic electrochemical behaviors analyzed by a three-electrode mode

To elucidate the function of the aforementioned electrode/membrane interface, we differentiated the anodic and cathodic polarization curves *via* a three-electrode mode to evaluate the individual contribution of each electrode (Fig. 2a). For the conventional C/C/C configuration, the cathode voltage decays rapidly from 0.35 V to −0.2 V upon the increase of current density from 0 to 1 A cm^{-2}. In contrast, the change in anode voltage is about 0.1 V, which is much smaller than that in the cathode. The large cathodic polarization loss renders DBFC performance limited by the cathode, which is consistent with those reports in the literature.[20] When AEM is employed, the

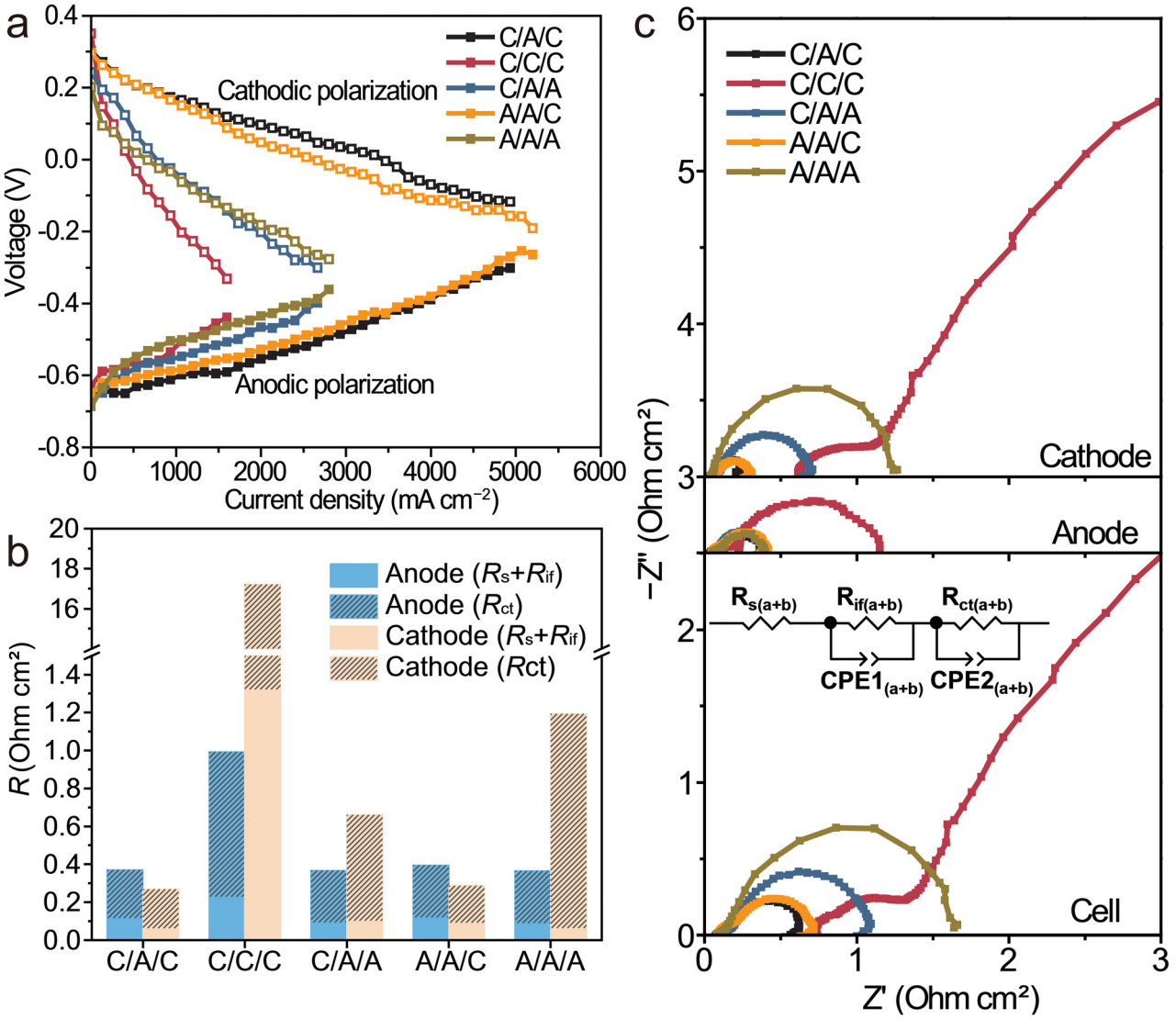

Fig. 2 Three-electrode characterization of DBFC. (a) Anode and cathode *I*–*V* polarization of DBFCs with different configurations. (b) Comparison of anode and cathode impedances based on the equivalent circuit model. (c) Nyquist plots of electrochemical impedance spectra (EIS) measured for the DBFCs with different configurations at the open circuit voltage. For clarity, the anode and cathode EIS were offset by 2.5 and 3 Ohm cm^2, respectively.

cathodic polarization is significantly mitigated. As compared with C/C/C, the maximum current density exceeds twice for A/A/A and C/A/A and 4 times for C/A/C and A/A/C. It is obvious that DBFCs with the cathode microscale bipolar interface have much better performance than other configurations. Note that Nafion® has a superior hydrophobic ability to AEI (Fig. S5, ESI†), which may also contribute to promoting the O_2 mass transport. Regarding the anode polarization curves, no remarkable difference has been observed for all the configurations. When the anode ionomer is the only variable, Nafion® can slightly decrease the anode polarization due to the mitigated BH_4^- hydrolysis compared with AEI. Such results also align with the order of the aforementioned OCV and peak power density with different configurations. Overall, C/A/C exhibits the most promising performance among all the configurations.

The three-electrode electrochemical impedance spectroscopy (EIS) measurements at OCV were also carried out to gain insights into the electrochemical properties of the anodes and cathodes simultaneously. The Nyquist plots for the anode, cathode and single cell are presented in Fig. 2b. For clarity, the anode and cathode EIS were offset by 2.5 and 3 Ohm cm^2, respectively. Both anode and cathode exhibit two distorted semicircles. The semicircle in the high-frequency region is associated with the interfacial impedance between the catalyst layer and membrane while the one in the intermediate frequency region can be ascribed to the electrochemical reactions within the catalyst layer. The equivalent circuit containing the internal resistance ($R_{s(a+c)}$), a parallel couple of $R_{if(a+c)}$/$CPE1_{(a+c)}$ corresponding to interfacial impedance, a parallel couple of $R_{ct(a+c)}$/$CPE2_{(a+c)}$ corresponding to electrochemical reaction impedance, was used to fit and analyze the EIS, where a and c stand for anode and cathode, respectively.[38] The resultant aforementioned parameters are summarized and compared in Fig. 2c. The overall resistance of the single cell consists of internal resistance and interfacial resistance ($R_{s(a+c)}$ + $R_{if(a+c)}$) which causes the Ohmic polarization while the charge transfer resistance ($R_{ct(a+c)}$) corresponds to the activation polarization. The conventional C/C/C configuration exhibits a cathode overall resistance of 1.32 Ω cm^2 and charge transfer resistance of 15.88 Ω cm^2, which are significantly reduced to 0.063 and 1.13 Ω cm^2 for A/A/A, 0.10 and 0.56 Ω cm^2 for C/A/A, 0.092 and 0.20 Ω cm^2 for A/A/C, and 0.062 and 0.21 Ω cm^2 for C/A/C, respectively (Table S1, ESI†). As a result, the cathode polarization of the conventional C/C/C configuration can be significantly reduced by the adoption of AEM and further by the cathode microscale bipolar interface. For the anode branch, all the configurations present similar or comparable overall and charge transfer resistances which are much smaller than those for the cathode branch of the conventional C/C/C configuration. In addition, the anode of the conventional C/C/C configuration shows slightly higher overall resistance and charge transfer resistance than the other configurations (*e.g.*, A/A/A, C/A/A, A/A/C, and C/A/C). Both the three-electrode EIS and polarization results elucidate that mitigating cathode polarization is the key to achieving high-performance DBFCs.

BH_4^- tolerance of the Mn–Co-BP2000 ORR cathode catalyst

Rotating disk electrode (RDE) measurements were conducted to investigate the BH_4^- tolerance of the Mn–Co-BP2000 ORR cathode catalyst. Fig. 3a and b show the effect of BH_4^- on cyclic voltammograms (CV) of Pt/C and Mn–Co-BP2000 catalysts under both Ar and O_2, respectively. In the absence of BH_4^-, Pt/C exhibits the typical potential regions for hydrogen adsorption and desorption, the double-layer capacitance region, and the formation and reduction of surface oxides under Ar.[39] As expected, Pt/C exhibits ORR activity below 1 V when O_2 saturates the electrolyte. In the presence of 10 mM BH_4^-, the oxidation current of BH_4^- dominates all the other reactions under both Ar and O_2. Conversely, BH_4^- has a slight effect on the CV of Mn–Co-BP2000 catalysts. In the Ar-saturated electrolyte, the redox peaks can be observed in the absence and presence of BH_4^-, which are ascribed to the redox couples of $Co^{+2/3}$ and $Mn^{+2/3/4}$ redox couples.[40] In the O_2-saturated electrolyte, Mn–Co-BP2000 apparently demonstrates ORR activity below 0.9 V. It is worth pointing out that the superposition of small BH_4^- oxidation current occurs above 0.85 V under both

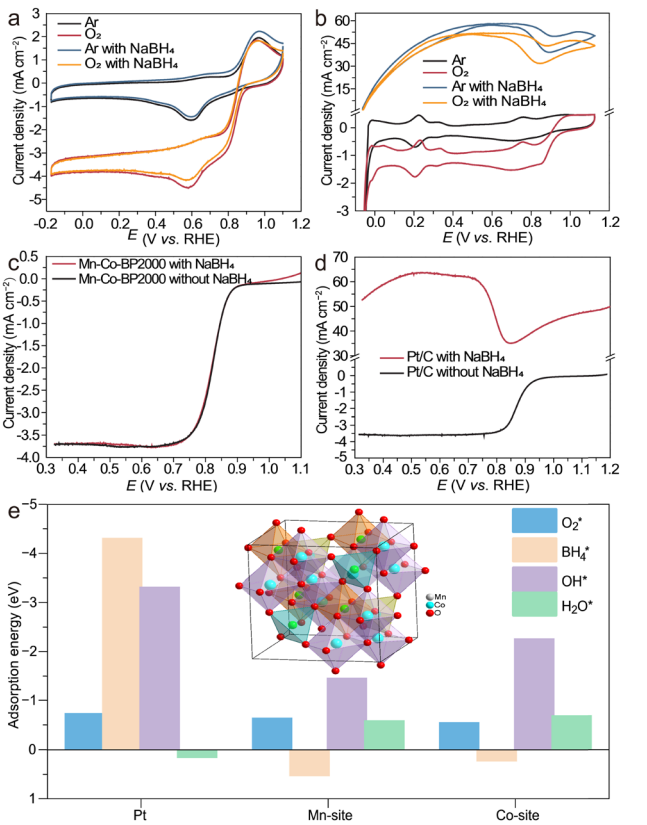

Fig. 3 $NaBH_4$ tolerance of Mn–Co-BP2000 cathode catalyst. Cyclic voltammetry (CV) of (a) Mn–Co-BP2000 and (b) Pt/C in Ar- and O_2-saturated 1 M KOH solution with the absence and presence of 10 mM $NaBH_4$. Linear sweep voltammetry (LSV) of (c) Mn–Co-BP2000 and (d) Pt/C in O_2-saturated 1 M KOH solution with the absence and presence of 10 mM $NaBH_4$. All the tests were carried out at 25 °C and 1600 rpm with a potential sweep rate of 20 mV s^{-1}. (e) Adsorption energies of H_2O, O_2, OH and BH_4 calculated by density functional theory (DFT) on the Mn and Co sites of the Mn–Co-BP2000 (100) surface and Pt (111).

Ar and O_2 when BH_4^- is added in the electrolyte. The BH_4^--tolerant ORR activity of Mn–Co-BP2000 was further verified by linear sweeping voltammograms (LSVs) in O_2-saturated electrolyte (Fig. 3c and d). The half-wave potentials ($E_{1/2}$) of Mn–Co-BP2000 were about 0.84 V in the absence and presence of BH_4^-. Consistent with the CV results, the BH_4^- oxidation current is also observed when the voltage goes above 0.85 V. Pt/C shows an $E_{1/2}$ of 0.86 V in the absence of BH_4^-, which is higher than that of Mn–Co-BP2000. However, the presence of BH_4^- conceals the ORR activity of Pt/C similar to CV results. Similar BH_4^--tolerant ORR properties of Mn–Co-BP2000 were also observed when Alkymer® is employed as the ionomer. Note that the ORR activity is higher with Nafion® as the ionomer due to its higher hydrophobicity and higher O_2 permeability.

To elucidate the aforementioned BH_4^- tolerance of the Mn–Co-BP2000 ORR catalyst, we conducted DFT calculations for the free energy of the intermediates of the ORR along with BH_4^- on the Mn and Co sites in comparison to those on Pt (Fig. 3e). Both O_2 and BH_4^- can be exothermically adsorbed on Pt with a much stronger Pt–BH_4^- interaction than the Pt–O_2 interaction. Consequently, the Pt electrode prefers to bind BH_4^- over O_2 and shows a favorable energy path of BOR[41] over ORR behavior in the O_2-saturated electrolyte containing BH_4^- (Fig. S6 and S7, ESI†). In contrast, the adsorption of BH_4^- on both Mn and Co sites of Mn–Co-BP2000 is energetically unfavorable while both sites present comparable O_2 absorption energies as Pt. As a result, Mn–Co-BP2000 can demonstrate ORR activity with BH_4^- tolerance in the O_2-saturated electrolyte containing BH_4^-. Furthermore, our calculations reveal that Mn sites have a higher O_2 adsorption energy and a more favorable energy path towards the ORR than Co sites, suggesting that Mn is more likely to act as the catalytic center (Fig. S7, ESI†).[42]

Mitigation of the crossover effect by the cathode microscale bipolar interface

Similar to other liquid fuel cells, borohydride crossover in DBFCs not only decreases fuel utilization but also causes parasitic current on the cathode, resulting in poor cell performance. As shown in Fig. 4a, the borohydride permeabilities through AEM and CEM membranes at 80 °C were measured using H-cell where the source compartment was filled with the anolyte of 1 M $NaBH_4$–3 M KOH solution and the receiver compartment contains 3 M KOH solution.[25] The borohydride concentration in the receiver compartment was obtained by extrapolating the optical absorbance at 350 nm against the calibration curve. In addition, Nafion® ionomer and poly(arylene piperidinium)-based AEI were cast into membranes for permeability evaluation. The permeabilities (Fig. 4b and c) are determined as 8.7×10^{-9} and 3.9×10^{-8} $cm^{-2}\ s^{-1}$ for CEM (Gore-select®) and CEI (Nafion®), and 8.8×10^{-7} and 9.3×10^{-7} $cm^{-2}\ s^{-1}$ for AEM and AEI, respectively. As expected, CEM (Gore-select®) and CEI (Nafion®) are more effective in suppressing the BH_4^- crossover than AEM and AEI. Such a difference is intimately related to their polymeric structure. The negatively-charged $-SO_3^{2-}$ side chains of CEM and CEI repulse BH_4^- crossover while the electrostatic

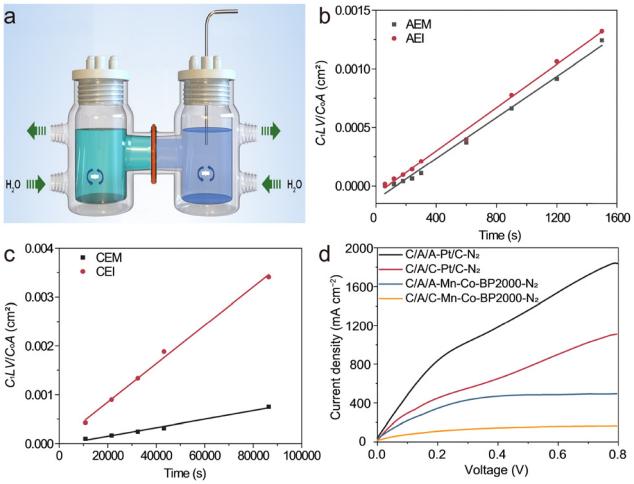

Fig. 4 BH_4^- permeability and permeated BH_4^- oxidation at the cathode. (a) Schematics for BH_4^- permeability measurement using concentration-driven dialysis diffusion H-cells at 80 °C. (b) and (c) Normalized BH_4^- concentration in the receiver compartment as a function of time for anion exchange membrane and ionomer (AEM and AEI) and cation exchange membrane and ionomer (CEM and CEI), respectively. (d) Linear sweep voltammetry for the oxidation of BH_4^- permeating through the anion exchange membrane under the same conditions for DBFC except that O_2 was replaced by N_2.

attraction between BH_4^- and the positively-charged piperidinium groups of AEM and AEI facilitate BH_4^- crossover. It is expected that the DBFCs with the cathode microscale bipolar interface integrate the advantages of CEI that limits BH_4^- penetration to the cathode catalyst and the AEM that can provide high OH^- conductivity without NaOH and KOH accumulation at the cathode.

To investigate the effect of the cathode microscale bipolar interface on the oxidation of permeated borohydride, LSV (Fig. 4d) measurements were carried out on DBFCs with different interfaces at the cathode (A/A and A/C) under N_2.[34] For both Pt/C and Mn–Co-BP2000 cathodes, the presence of a cathode microscale bipolar interface (A/C) significantly decreases the current density of BH_4^- oxidation. Compared with Pt/C, Mn–Co-BP2000 exhibits lower BH_4^- oxidation current in both cases. The combination of the cathode microscale bipolar interface and BH_4^--tolerant Mn–Co-BP2000 cathode catalyst significantly mitigates the parasitic BH_4^- oxidation current from 1838 mA cm^{-2} at 0.8 V for the Pt/C cathode without a cathode microscale bipolar interface to 158 mA cm^{-2}. Harmonizing with the three-electrode EIS and polarization characterization, such results have interpreted the origin of the high-performance DBFC with the C/A/C configuration.

Optimization of DBFC performance

The effect of operation conditions (*e.g.*, KOH concentration, $NaBH_4$ concentration, cathode relative humidity, and temperature) on cell performance was systematically investigated. To optimize $NaBH_4$ concentration, the KOH centration was maintained at 3 M while $NaBH_4$ concentration varied from 0.6 to 1.4 M in the fuel solution. As shown in Fig. S8 (ESI†), 1 M

$NaBH_4$ in the fuel solution resulted in the highest peak power density of 1539.5 mW cm^{-2}. When the $NaBH_4$ concentration increased from 1 to 1.4 M, the degradation of peak power density was possibly ascribed to the increase of $NaBH_4$ crossover. Adding KOH alkali in the fuel solution not only alleviates the hydrolysis of $NaBH_4$ but also improves the $NaBH_4$ electrooxidation kinetics. It was found that the peak power density of DBFC increased from 1266.5 to 1539.5 mW cm^{-2} when the KOH concentration increased from 1 to 3 M (Fig. S9, ESI†). However, the peak power density decreased to 1183.4 mW cm^{-2} when the KOH concentration increased to 5 M. As reported in the literature,[7,43] too high alkali concentration can cause a high viscosity of the fuel solution, lowering the effective diffusivity of borohydride ions and thus increasing the transport resistance of borohydride. Too high alkali concentration can also cause the majority of the reaction sites occupied by hydroxide ions, mismatching two reactants and thus lowering the anodic kinetics. Besides KOH and $NaBH_4$ concentrations, it is necessary to compromise the relative humidity (RH) of O_2 since water is not only a reactant in the ORR but also prevents O_2 transport under flooding conditions. It turns out that better performance has been achieved under RH of 80% than those at 60% and 100% when the DBFCs were operated at 80 °C (Fig. S10, ESI†). The DBFC performance is highly dependent on cell operating temperature. The kinetics of both ORR and BOR improve with the increase of temperature. The conductivity and diffusivity of the analyte solution also increase with increasing temperature, which can mitigate the ohmic and concentration polarizations, respectively. As shown in Fig. 5a, the peak power density increases from 287 to 1539.5 mW cm^{-2} and the current density corresponding to peak power density increases from 660 to 3058 mA cm^{-2} as the cell temperature was increased from 25 to 80 °C. When the temperature was elevated above 80 °C, borohydride hydrolysis and crossover rates along with the membrane instability increased, resulting in a deteriorated performance with a lower peak power density of 1430 mW cm^{-2} at 90 °C (Fig. S11, ESI†). Therefore, the optimum operation conditions were identified as the analyte of 1 M $NaBH_4$ in

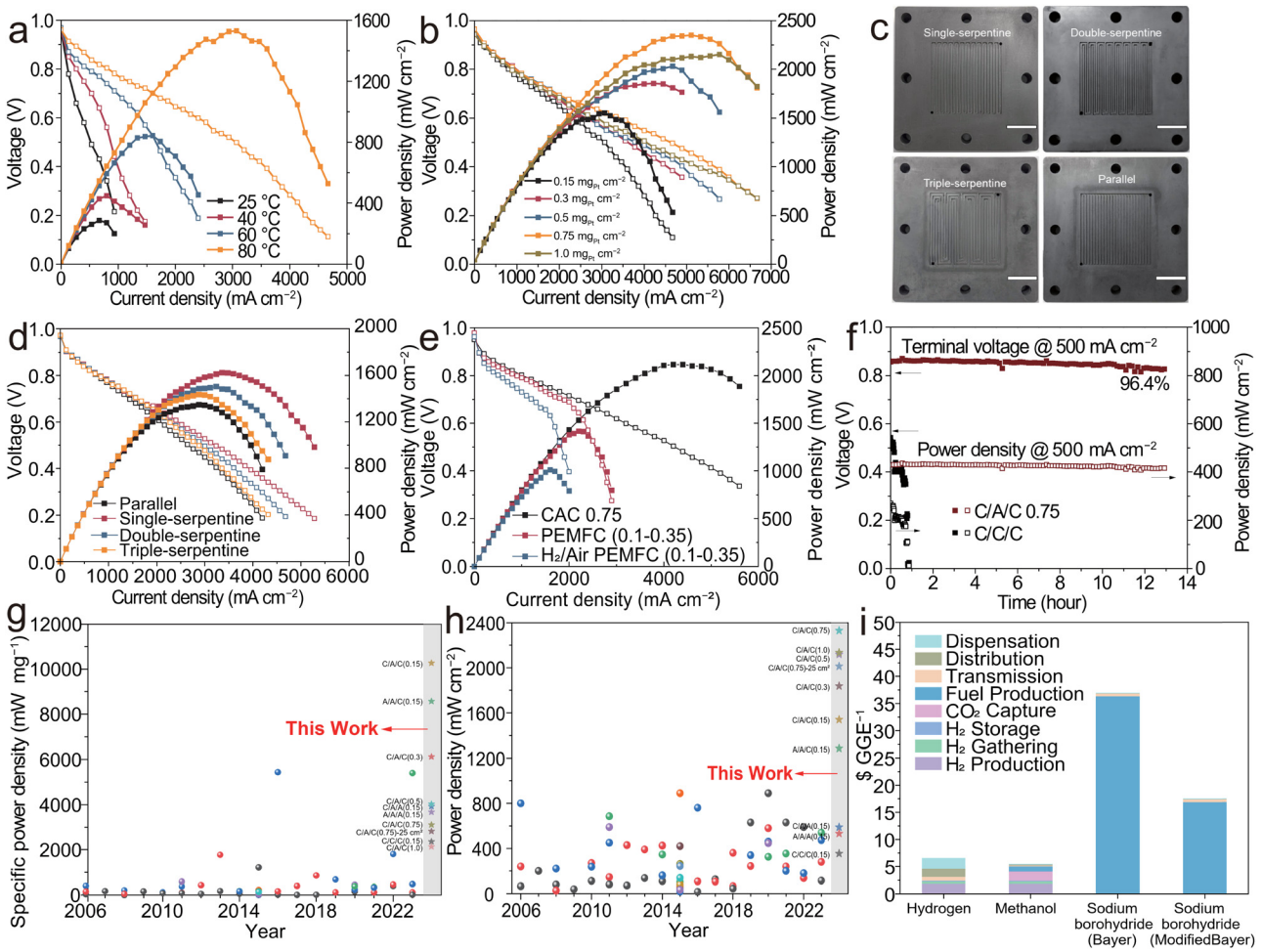

Fig. 5 DBFC optimization, scale-up, durability and comparison with PEMFC. *I–V* polarization and power density of DBFCs at different (a) operating temperatures and (b) Pt loadings. (c) Photograph and (d) DBFC performance of parallel, single serpentine, double serpentine, triple serpentine flow fields with the active area of 5 × 5 cm^2. (e) Comparison of DBFC with commercial PEMFCs operated under H_2–air and H_2–O_2. (f) DBFC cell durability test. Comparison of (g) noble metal-mass specific power density and (h) areal peak power density with literature reports. (i) Source-to-tank energy cost comparison of hydrogen, methanol and sodium borohydride. The unit is normalized to $ GGE^{-1}.

3 M KOH solution, RH of 80% and temperature of 80 °C, which were used in all other evaluations unless otherwise specified. The aforementioned cell electrochemical tests were all applied to the DBFCs with 0.15 mg_{Pt} cm^{-2} as the anode, 1.5 mg cm^{-2} Mn–Co-BP2000 as the cathode and 15 μm AEM as the electrolyte which serves as the base for cell structure optimization.

Besides the operation conditions, the cell structures including catalyst loading, membrane, and anode catalyst were further investigated to improve the performance of DBFCs. Fig. 5b shows that a record-breaking peak power density of 2330.7 mW cm^{-2} has been achieved for the DBFC with a Pt loading of 0.75 mg cm^{-2} and Mn–Co-BP2000 loading of 1.5 mg cm^{-2} due to the tradeoff among the increasing accessible reaction sites, the reduced mass transport and increasing resistance upon increasing the catalyst loading.[44] Increasing the AEM thickness from 15 to 25 μm leads to the decrease of peak power density from 1539.5 to 1300 mW cm^{-2} due to the increased resistance (Fig. S13, ESI†). When the anode catalyst Pt/C in C/A/C was replaced by PtIr/C (Fig. S14, ESI†), a similar performance was obtained under the same operation conditions. It is worth mentioning that the peak power density at 25 °C was improved from 287 mW cm^{-2} for Pt/C to 351 mW cm^{-2} for PtIr/C. Such an improvement can be ascribed to the moderately higher BOR activity of PtIr/C compared with that of Pt/C, indicated by CV curves at 25 °C (Fig. S15, ESI†). All results indicate that further improvement of the DBFC performance intimately depends not only on the operation conditions but also on the key materials and cell configurations.

DBFC scale-up and its comparison with PEMFCs

It is not trivial to translate the promising performance of single cells with a small active area to those with a large active area. Four different flow fields (*e.g.*, parallel, single serpentine, double serpentine, triple serpentine) with an active area of 5 × 5 cm^2 (Fig. 5c) were adopted to scale up the aforementioned 1.5 × 1.5 cm^2 base DBFC with a Pt loading of 0.15 mg cm^{-2}. The peak power densities of 1.35, 1.43, 1.50, and 1.62 W cm^{-2} for parallel, triple serpentine, double serpentine, and single serpentine flow fields, respectively (Fig. 5d). When a single serpentine flow field is used, the 5 × 5 cm^2 optimum DBFC with a Pt loading of 0.75 mg cm^{-2} (Fig. S16, ESI†) can deliver a peak power density of 2.1 W cm^{-2} at 0.50 V at an O_2 flow rate of 1.0 NLPM (Fig. 5e), which is comparable to that of the small counterpart. For comparison, the commercial 5 × 5 cm^2 PEMFCs were also evaluated with the same air or O_2 flow rate as that used for DBFCs. The H_2/air and H_2/O_2 PEMFCs can deliver peak power densities of 1.0 W cm^{-2} at 0.63 V and 1.42 W cm^{-2} at 0.64 V, respectively, whereas a higher power density of 1.79 W cm^{-2} at 0.64 V is obtained for the DBFC. Additionally, the effect of the O_2 flow rate on the DBFC was investigated. The peak power density is improved by increasing O_2 flow rate from 0.6 to 1.4 NLPM (Fig. S17, ESI†). It is worth mentioning that a flow rate of greater than 0.6 NLPM is entailed due to the high current density of approximately 6 A cm^2. However, a high flow rate can escalate pressure drop (Fig. S18a, ESI†), leading to nonuniform distribution of O_2 concentration and high power consumption of the auxiliary components (*e.g.* the air compressor).[45,46] The pressure drop can be effectively mitigated by increasing the number of channels, whereby the length of each channel is diminished. As shown in Fig. S18b (ESI†), the pressure drops at the flow rate of 1.0 NLPM decrease from 30.7 to 1.5 kPa in the order of single serpentine, double serpentine, flow triple serpentine and parallel flow field. In particular, when the flow field changes from single to double serpentine, the pressure drop can be decreased by 67% while the peak power density only diminishes by 7.4%. Therefore, high performance and large area DBFC with a low pressure drop can be achieved through the design of flow field.

Furthermore, the DBFC durability was evaluated by monitoring the voltage changes in the cell during galvanostatic discharge (Fig. 5f and Fig. S19, ESI†). The conventional DBFC with C/C/C configuration shows that both power density and output voltage decay rapidly to zero within 0.8 hours. Conversely, the power density shows slight attenuation at a constant current of 500 mA cm^{-2} after 12 hours and is maintained above 415 mW cm^{-2} along with the voltage retention of 96.4%, suggesting that the cell has good stability (Fig. 5f). It was found that the voltage retention would decrease when the Pt/C loading at the anode was reduced. Postmortem analysis was employed to investigate the structural evolution of the Pt/C anode and Mn–Co-BP2000 cathode during durability testing. SEM images of the anodes (Fig. S20, ESI†) display slight detachment of the Pt/C catalyst from the carbon fibers. Both TEM and STEM images (Fig. S21–S23, ESI†) further indicate that sintering and loss of Pt nanoparticles occurred during the durability test. The nanoparticles were expelled from the carbon substrate by the formed carbonates, indicated by the XRD (Fig. S24, ESI†), XPS (Fig. S25, ESI†) and elemental mapping results. As for the Mn–Co-BP2000 cathode, more cracks were observed after the durability test and the catalyst layer became thicker (Fig. S26 and S27, ESI†). The crystallinity of the cubic spinel Mn–Co-BP2000 in the tested electrode becomes weaker than that in the pristine cathode (Fig. S28, ESI†). As revealed by TEM and STEM results (Fig. S29–S33, ESI†), the spinel oxide nanoparticles are agglomerated after the durability test and the proportion of small nanoparticles has decreased. The quantitative analysis of the XPS results (Fig. S34, S35 and Table S2, ESI†) shows the increase of the Co/Mn ratio from 1 to 1.3, indicating the Mn dissolution during the durability test.[47] Additionally, the tested sample presents decreased atomic ratios of Mn^{3+}/Mn^{2+} and Co^{3+}/Co^{2+}, which can be ascribed to the reduction of spinel Mn–Co-BP2000 by the permeated BH_4^-. All these factors contribute to the performance deterioration of the DBFCs during the durability test.

Fig. 5g and h compare the DBFC peak powers in our work with the typical values from the literature (Table S3, ESI†), which are normalized to Pt loading and cell area. The areal peak power density shows a significant enhancement and surpasses 2 W cm^{-2} for the first time, which is the highest value for DLFCs (*e.g.*, methanol, ethanol, hydrazine, ammonia, formic acid, ethylene glycol, dimethyl ether, *etc.*). The peak power density of DLFCs is usually limited to below 1 W cm^{-2}

due to their much slower reaction kinetics of liquid fuel oxidation than that of hydrogen oxidation in PEMFCs.[4,48] The mass-specific PPD based on Pt loading is a critical characteristic catalyst activity parameter that intimately shapes the catalyst cost in the fuel. As shown in Fig. 5h, the highest mass-specific PPD in this work reaches 10.2 kW g^{-1}. This means the total platinum group metal total content (both electrodes) in this work decreases to 0.098 g kW^{-1}, which is even lower than the 2020 U.S. Department of Energy (DOE) target of 0.125 g kW^{-1} set for PEMFC-rated power.[49] Such comparison further corroborates the unprecedented performance of DBFCs achieved in this work. Furthermore, the source-to-tank energy cost of sodium borohydride normalized to gasoline gallon equivalent (GGE) and mass (kg) was analyzed and compared with those of hydrogen and methanol (Fig. 5i, Fig. S36–S40 and Tables S4–S9, ESI†). The source-to-tank energy cost of sodium borohydride including the Bayer process ($37.02 GGE^{-1}) and the modified Bayer process ($17.52 GGE^{-1}) is significantly higher than that of hydrogen ($6.55 GGE^{-1}) and methanol ($5.46 GGE^{-1}). Such a high cost of sodium borohydride is ascribed to the high production cost ($36.32 GGE^{-1} for the Bayer process and $16.88 GGE^{-1} for the modified Bayer process), where high cost reducing metals are used as the raw materials. For the Bayer process and the modified Bayer process, the cost of reduction metals accounts for 79% and 62.2% of the raw material, respectively (Fig. S38, ESI†). The sodium borohydride production cost can be further reduced if the production process is implemented using other cheaper reducing metals (such as aluminum).[50]

Conclusions

In conclusion, we have demonstrated high-performance low-temperature DBFCs by mitigating cathode polarization. The three-electrode and fuel crossover studies indicate that the cathode microscale bipolar interface and non-noble cathode catalyst significantly suppress the BH_4^- oxidation at the cathode. Such DBFCs can deliver unprecedented peak power densities of greater than 2 W cm^{-2} at 80 °C. As compared with PEMFCs, the compact fuel cartridge and high performance ranging from ambient temperature to 80 °C make the DBFCs an attractive power source for portable devices, drones and unmanned underwater vehicles. The low Pt loading and anion exchange membrane significantly decrease the DBFC cost. The technoeconomic analysis indicates the DBFC cost is dominated by the production cost of sodium borohydride which can be reduced by using cheaper reducing metals. The high performance of 5 × 5 cm^2 DBFC paves the way to make stacks and explore their practical applications.

Experimental

Chemicals and materials

All the deionized water used in this study was produced from a Milli-Q system (18.2 MΩ cm). BLACK PEARLS®2000 carbon black (BP2000) was obtained from Cabot. Nitric acid (HNO_3, 65–68%), manganese(II) acetate tetrahydrate [$Mn(OAc)_2{\cdot}4H_2O$, 99%], cobalt(II) acetate tetrahydrate [$Co(OAc)_2{\cdot}4H_2O$, 99.5%], ammonia aqueous ($NH_3{\cdot}H_2O$, 25–28%), potassium hydroxide (KOH, 85%), sodium borohydride ($NaBH_4$, 96%), and isopropanol (99.7%) were purchased from Sinopharm Chemical Reagent Co., Ltd. Nicotinamide adenine dinucleotide (NAD^+, 99%) was purchased from Adamas-beta®. Borate buffered saline (0.05 M, pH of 8.5) was purchased from Phygene Biotechnology Co., Ltd. Commercial Pt/C (40%, Johnson Matthey Co.), commercial PtIr/C (40 wt%, Pt : Ir = 1 : 1, Johnson Matthey Co.), cation exchange ionomer Nafion® (Dupont, 5 wt%), and anion exchange ionomer Alkymer® I-250 (EVE Institute of New Energy Sources, 5 wt%) were used as received. The cation exchange membrane Gore-select® (18 μm) was obtained from W. L. Gore & Associates, Inc. The anion exchange membrane Alkymer® W-211415 (15 μm) and W-25 (25 μm) were obtained from EVE Institute of New Energy Technology. The membrane electrode assembly (MEA) of the proton exchange membrane fuel cell was purchased from Henan Yuqing Power Co., Ltd, which has 0.1 and 0.35 mg_{Pt} cm^{-2} in the anode and cathode, respectively.

Synthesis of Mn–Co-BP2000 spinel cathode catalyst

For chemical modification of the carbon support, 2 g BP2000 was firstly dispersed in 100 mL HNO_3. Afterwards, the suspension was heated to 70 °C and maintained for 2 hours under magnetic stirring. Then, the suspension was cooled to room temperature. Thereafter, the suspension was centrifugated and washed using deionized water repeatedly until the supernatant became neutral. Finally, the modified BP2000 was obtained by freeze drying.

The synthesis of the Mn–Co-BP2000 spinel catalyst is reported as previously described in detail.[29,42] Typically, 63.5 mg of $Co(OAc)_2{\cdot}4H_2O$ and 60 mg of pre-oxidized carbon support were dispersed in 30 mL of deionized water within a breaker and homogenized under sonication for 30 min. Then, the uniform solution was transferred to a heating oil bath at room temperature and 0.5 mL of $NH_3{\cdot}H_2O$ was added dropwise into the solution under magnetic stirring, followed by ramping the oil bath to 60 °C. Afterwards, an aqueous solution of 62.5 mg $Mn(OAc)_2{\cdot}4H_2O$ in 5 mL deionized water was added. After aging for 2 hours, the resulting suspension was sonicated, transferred into a 100 mL Teflon-lined stainless-steel autoclave, and reacted at 150 °C for 3 hours. Finally, the mixture was cooled naturally to room temperature, washed with deionized water for several times, and freeze-dried for 12 hours to obtain the Mn–Co-BP2000 spinel catalyst.

Fabrication of single cells

In our study, 40 wt% Pt/C and Mn–Co spinel were used as the anode and cathode catalysts, respectively. Both anode and cathode catalyst inks were prepared similarly. Typically, the catalyst powder was dispersed into isopropanol with the concentration of 5 mg mL^{-1} under ultrasonication in an ice bath for 30 min. Then, Nafion® (the catalyst/Nafion® mass

ratio is 3 : 1) was added into the solution and sonicated for another 30 min. The anode and cathode catalyst inks were sprayed using an airbrush onto carbon cloth (W0S1009, Ce Tech Co., Ltd, Taiwan) and carbon paper (28BC, SGL Carbon, Wiesbaden, Germany), respectively. The effective area of anode and cathode electrodes was 1.5 × 1.5 or 5 × 5 cm^2. The Pt loading at the anode was *ca.* 0.15 mg cm^{-2}, and the Mn–Co spinel catalyst loading at the cathode was *ca.* 1.5 mg cm^{-2}. Furthermore, the poly(arylene piperidinium) based anion exchange membranes (Alkymer®) were used as an electrolyte to separate anode and cathode reactants. The membranes were immersed in 2 M KOH aqueous solution for 24 hours to replace Cl^- with OH^- at 60 °C. Before MEA fabrication, the membranes were thoroughly rinsed using deionized water to remove the residual KOH and KCl. The single cells were fabricated by sandwiching the membrane with the anode and the cathode, followed by contacting their rear with two graphite flow fields for anolyte and oxygen, respectively. For 1.5 × 1.5 cm^2 fuel cell, a single-channel serpentine flow field was used for the liquid anolyte transport and a double-channel serpentine flow field was used to guide oxygen. For the 5 × 5 cm^2 fuel cell, a triple-channel serpentine flow field was used in the anode side and a single-channel serpentine flow field was used to guide oxygen. Silicone sheets with a thickness of 200 and 300 μm were used as the cathode and anode gaskets, respectively. Finally, a torque of 6 N m was applied to seal the cell.

Evaluation of single cell performance

The DBFC performance was measured by a fuel cell test station (G20, Greenlight Innovation Corp. Canada). Before measurements, N_2 gas and 1 M KOH aqueous solution were employed to flush the cathode and anode flow fields, respectively. When the testing temperature was stable, the oxygen and anolyte (3 M KOH + 1 M $NaBH_4$) feeds were supplied to the cathode and anode, respectively. The oxygen was supplied with a flow rate of 0.5 NLPM at an inlet temperature of 80 °C and a relative humidity (RH) of 80% without back pressure. The anolyte was heated 80 °C by an oil bath and transported to the flow field by a peristaltic pump at a flow rate of *ca.* 5 mL min^{-1}. The cell temperature was maintained at 80 °C through an electronic thermostat. For the 5 × 5 cm^2 fuel cell, the flow rate of oxygen and anolyte increased to 1.0 NLPM and 80 mL min^{-1}, respectively.

The single cells were initially activated by a current density of 500 mA cm^{-2} until the voltage became stable. The fuel cell polarization curves were acquired by stepping the current from zero to the maximum test current with an increment of 300 mA. The maximum test current corresponded to the cell voltage that went below 0.2 V. Each current density was held for 30 seconds. The durability tests were conducted by chronopotentiometry scan at 500 mA cm^{-2} for approximately 12 hours.

Electrochemical characterization of single cells by a three-electrode mode method

A three-electrode setup with silver (Ag) as the pseudo-reference electrode was employed to identify the individual contribution of the anode and cathode to the single cell. One end of an Ag strip with a thickness of 0.05 mm, width of 0.2 cm, and length of 6 cm was attached to the edge of the membrane by thin polyimide tape. The other end was extended outside of the cell for electrical connection. During the operation of DBFC single cells, both anode and cathode voltages *versus* the Ag pseudo-reference electrode were recorded by digital voltmeters. The electrochemical impedance spectroscopy (EIS) of the anode, cathode and single cell were simultaneously collected at open circuit voltage using an electrochemical workstation (Biologic VMP3, France), and analyzed by the ZView software.

Electrochemical characterization of anode and cathode catalysts

The electrochemical characterization of Pt/C (or PtIr/C) and Mn–Co spinel catalysts were conducted in a three-electrode configuration using a CH Instruments 760E workstation with a rotating disk electrode (Pine Research Instruments). A 1.0 M KOH saturated Hg/HgO electrode and graphite rod were used as the reference and counter electrodes in a 250 mL jacketed glass cell, respectively. For the preparation of working electrodes, 6 mg of catalyst powder was uniformly dispersed in the mixing solution of 3 mL isopropanol and 60 μL Nafion® under sonication in an ice bath for 1 h. A 10 μL aliquot of the homogenous ink was pipetted and deposited onto the top of the polished glassy carbon RDE (5 mm in diameter, geometric area 0.196 cm^2) and dried at room temperature. For the borohydride oxidation reaction (BOR), cyclic voltammetry was carried out on the commercial Pt/C and PtIr/C electrodes in the freshly prepared 1 M KOH with 10 mM $NaBH_4$ electrolyte at 25 °C under an Ar atmosphere.

To investigate the effect of the borohydride on the oxygen reduction reaction (ORR) at the cathode, we conducted cyclic voltammetry (CV) in 1.0 M KOH supporting electrolyte at 25 °C, with the presence or absence of 10 mM $NaBH_4$. The CV tests were conducted at a sweep rate of 50 mV s^{-1} in Ar/O_2 statured electrolyte. Furthermore, the linear scanning voltammogram (LSV) tests were conducted at a sweep rate of 20 mV s^{-1} with a rotational speed of 1600 rpm in O_2 statured electrolyte. All potentials in this study were converted to the reversible hydrogen electrode (RHE).

Measurement of $NaBH_4$ permeability

An H-cell with two reservoirs was applied to measure the permeability of the ion exchange membrane at 80 °C. One reservoir was filled with the 50 mL electrolyte (3 M KOH + 1 M $NaBH_4$) as the source compartment, and the other was filled with 50 mL 3 M KOH solution as the receiver compartment. Both compartments were separated by the membrane with an effective permeate area of 1.767 cm^2. The H-cell was connected to a heating bath circulator to maintain the two compartments at 80 °C which was the same as the operation temperature for DBFCs. To determine the amount of the $NaBH_4$ that crossed over the membrane quantitatively, a spectrophotometric method was used.[25,51] In detail, 1 mL of 30-fold dilution from the receiver compartment and 9 mL of the mixture containing

0.9 mL of 0.05 M NAD^+ and 8.1 mL of 0.05 M borate buffered saline reacted for 30 min at room temperature. Then the absorbance of the product was measured at a wavelength range between 380 and 320 nm against 0.1 M KOH blank by a UV-vis spectrophotometer (PerkinElmer LAMBDA 650, USA). The maximum absorbance at 350 nm is linear with borohydride concentration when the borohydride concentration is relatively low. We measured the absorbance of the standard solution of 0.2, 0.4, 0.6, 0.8 and 1.0 mM $NaBH_4$ in 0.1 M KOH and established the relationship between the maximum absorbance and borohydride concertation by linear fitting. Based on the linear relationship, the borohydride concentration in the receiver compartment was obtained and the permeabilities (P) were calculated according to the following equation:

$$P = \frac{C_1 L V}{C_0 A \Delta t} \quad (1)$$

where L is the membrane thickness (cm), V is the volume of receiver compartment (mL), C_0 is the initial borohydride concentration (M), C_1 is the borohydride concentration (M) measured for the receiver compartment, A is the permeate area (cm^2), and Δt is the permeate time (s).

Evaluation of permeated BH_4^-

To evaluate the BH_4^- crossover from the anode to cathode in the DBFCs, we changed the cathode supply from oxygen to nitrogen with the same flow rate, temperature, and humidity as those employed to operate the DBFCs. The linear sweeping voltammograms starting from 0 V towards higher voltage were applied to the DBFCs at a sweep rate of 20 mV s^{-1} to record the oxidation currents of the permeated BH_4^- at the cathode.

Optimization of DBFC performance

To optimize the operation conditions, variations in $NaBH_4$ concentration, KOH concentration, cathode oxygen RH, and temperature were applied to the DBFCs with 0.15 mgPt cm^{-2} as the anode, 1.5 mg cm^{-2} as the cathode and 15 μm AEM. Thereinto, the $NaBH_4$ concentration was varied from 0.6 to 1.4 M in the fuel solution while the KOH centration was maintained at 3 M. The KOH concentration increased from 1 to 5 M while the $NaBH_4$ concentration was kept at 1 M. After the anolyte was optimized as 1 M $NaBH_4$ + 3 M KOH, RHs of O_2 ranging from 60% to 100% were investigated. In addition, the effect of operation temperature on the DBFCs was explored from 25 to 90 °C.

Besides the operation conditions, the DBFC structure was manipulated to improve their performance, such as Pt/C loading varying from 0.15 to 1 mg_{Pt} cm^{-2}, Mn–Co spinel loading from 0.5 to 2.5 mg cm^{-2}, membrane thickness of 15 and 25 μm, and anode catalyst Pt/C and PtIr/C. Within 5 × 5 cm^2 fuel cells, through monitoring the pressure drops and polarization properties, various flow fields, including single-serpentine, double-serpentine, triple-serpentine, and parallel flow fields, and varying flow rates of 0.6 to 1.4 NLPM were evaluated. The DBFCs were operated with anolyte of 1 M $NaBH_4$ + 3 M KOH and 80% RH of O_2 at 80 °C.

Evaluation of proton exchange membrane fuel cell (PEMFC) performance

The performance of H_2–O_2 PEMFCs constructed from commercial MEA was evaluated by a fuel cell test station (G20, Greenlight Innovation Corp. Canada). Both cathode and anode flow fields were double-serpentine flow fields. The test conditions were specified as a flow rate of 0.5 NLPM, RH of 100%, back pressure of 150 kPa for H_2 and O_2, and cell temperature of 80 °C. After the PEMFC was activated, the polarization curve was collected under galvanic control with stepping the current density from zero to the maximum test current with an increment of 0.1 A cm^{-2} until the voltage went below 0.3 V. Each current density was held for 30 seconds. For the test of H_2–air PEMFCs, the flow rate of air was changed to 1.5 NLPM while the other conditions were kept identical as those applied in H_2–O_2 PEMFC.

Materials characterization

The plane-view and cross-section morphology of anode and cathode catalyst layers was observed by a scanning electron microscope (FEI quanta feg250, USA). The morphology and elemental composition of catalysts were characterized by a transmission electron microscope (TEM, FEI TalosF200x, USA), including high-resolution TEM (HRTEM), high-angle annular dark-field scanning TEM (HAADF-STEM) and energy-dispersive X-ray spectrometry (EDS) elemental mapping (Thermo Fisher Scientific Super-X EDS, USA). The crystal phases of catalysts were identified *via* powder X-ray powder diffraction (XRD, Rigaku Ultima IV, Japan) with Cu Kα X-rays. X-ray photoelectron spectroscopy (XPS, Thermo Fisher Scientific K-Alpha, USA) spectra were recorded to analyze the surficial atomic ratios. The degree of hydrophobicity of Nafion and Alkymer® I-250 was analyzed by the contact angles of their cast films using a contact angle measuring instrument (OCA20, Dataphysics, Germany).

Computational methods

Density functional theory (DFT) calculations were carried out by using the Vienna ab initio Simulation Package (VASP)[52,53] with the Perdew–Burke–Ernzerhof (PBE) exchange correlation functional of generalized gradient approximation (GGA) and projector augmented wave pseudopotentials (PAW).[54,55] The cut-off energy was set as 520 eV for the plane-wave basis set. The Monkhorst–Pack scheme was used to sample the Brillouin zone with a k-point mesh of 3 × 3 × 1. To accurately characterize the localization of the strongly correlated transition metal 3d-electrons of Mn–Co spinel, the DFT+U method was employed, incorporating the Hubbard U parameter.[56] The Hubbard U values of Mn and Co atoms were chosen as 4.4 eV and 5.4 eV, respectively.[57] The vacuum layer was 15 Å to guarantee negligible interactions between the periodically repeated slabs. Second-order Methfessel–Paxton smearing with a width of 0.1 eV was applied for setting partial occupancies. During geometry optimization, the adsorbate layer and the top half of the layers of the slab were allowed to relax. The energies

obeyed the criteria of total energy for the electron self-consistent field and force are 10^{-6} eV and -0.02 eV Å^{-3}.

A four-layer 4 × 4 orthogonal (111) slab was designed to simulate pure Pt, considering that (111) is the most dominantly exposed plane supported by the experimental data. For the reasonable calculation of surface and chemisorption systems, the Mn–Co spinel (100) surface was constructed as an eight-layer atom slab.[58] The valence states of Mn and Co were allowed to vary in the MCS system through reasonable position interchange of Mn and Co. The cations occupying the octahedral sites were considered as the main surface exposure sites when the surface was constructed, and the adsorbed species on Mn and Co sites were considered simultaneously to facilitate comparison and draw reasonable conclusions.

The potential dependence of reaction free energies in elementary steps involving proton–electron transfers was evaluated using the computational hydrogen electrode (CHE) method.[59] In this approach, a reversible hydrogen electrode (RHE) is used as a reference. The Gibbs free energy is calculated using $\Delta G = E_{DFT} + \Delta ZPE - T\Delta S$. Where G is the Gibbs free energy, E_{DFT} is the electronic energy from DFT calculations, ZPE is zero-point energy, and T is the temperature of 300 K. To determine the ORR performance, the adsorption energies of adsorbates were calculated based on the following equation: $E_{ads} = E_{total} - E_{slab} - E_{adsorbate}$, where E_{ads} is the adsorption energy, E_{total} is the total energy of the system with adsorbate, E_{slab} is the energy of the optimized slab, and $E_{adsorbate}$ is the energy of the isolated adsorbate in the gas phase.

Author contributions

Q. X. conceived the idea for the project. Y. G. prepared the materials and performed DFT calculations. Y. G. and F. G. performed the single fuel cell studies and three-electrode experiments. Y. G. and Y. J. C. performed the membrane/ionomer and NaBH4 permeability characterizations. F. G. and Z. H. assisted with MEA design and fabrication. Z. H. and C. Z. built the test stations. Y. H. interpreted the electrochemical impedance spectroscopy results. Q. T. performed the SEM, TEM, XRD, and XPS characterizations. C. Z. assisted in data analysis. Y. H. and Y. Z. carried out technoeconomic analysis. Q. X. and Y. C. supervised the execution of the overall project. Q. X. and Y.G. drafted the manuscript. All authors discussed the results.

Data availability

The data supporting the findings of this study are available within the article and its ESI.†

Conflicts of interest

There are no conflicts to declare.

Acknowledgements

This research was supported by Clean Energy Automotive Engineering Center of Tongji University for fundamental study. We thank P. M., B. L., and D. Y. from Tongji University for their experimental assistance.

Notes and references

1 J. Kunze and U. Stimming, *Angew. Chem., Int. Ed.*, 2009, **48**, 9230–9237.
2 K. Jiao, J. Xuan, Q. Du, Z. Bao, B. Xie, B. Wang, Y. Zhao, L. Fan, H. Wang, Z. Hou, S. Huo, N. P. Brandon, Y. Yin and M. D. Guiver, *Nature*, 2021, **595**, 361–369.
3 Y. Wang, Y. Pang, H. Xu, A. Martinez and K. S. Chen, *Energy Environ. Sci.*, 2022, **15**, 2288–2328.
4 N. Shaari, S. K. Kamarudin, R. Bahru, S. H. Osman and N. A. I. Md Ishak, *Int. J. Energy Res.*, 2021, **45**, 6644–6688.
5 B. C. Ong, S. K. Kamarudin and S. Basri, *Int. J. Hydrogen Energy*, 2017, **42**, 10142–10157.
6 J.-H. Wee, *J. Power Sources*, 2006, **161**, 1–10.
7 J. Ma, N. A. Choudhury and Y. Sahai, *Renewable Sustainable Energy Rev.*, 2010, **14**, 183–199.
8 H. X. Nunes, D. L. Silva, C. M. Rangel and A. M. F. R. Pinto, *Energies*, 2021, **14**, 3567.
9 M. C. S. Escaño, E. Gyenge, R. L. Arevalo and H. Kasai, *J. Phys. Chem. C*, 2011, **115**, 19883–19889.
10 C. P. de Leon, F. C. Walsh, D. Pletcher, D. J. Browning and J. B. Lakeman, *J. Power Sources*, 2006, **155**, 172–181.
11 S. Li, Y. Liu, Y. Liu and Y. Chen, *J. Power Sources*, 2010, **195**, 7202–7206.
12 J. Yu, B. Hu, C. Xu, J. Meng, S. Yang, Y. Li, X. Zhou, Y. Liu, D. Yu and C. Chen, *Dalton Trans.*, 2021, **50**, 10168–10179.
13 B. H. Liu and S. Suda, *J. Power Sources*, 2007, **164**, 100–104.
14 R. Sgarbi, E. A. Ticianelli, F. Maillard, F. Jaouen and M. Chatenet, *Electrocatalysis*, 2020, **11**, 365–373.
15 C. Grimmer, M. Grandi, R. Zacharias, S. Weinberger, A. Schenk, E. Aksamija, F.-A. Mautner, B. Bitschnau and V. Hacker, *J. Electrochem. Soc.*, 2016, **163**, F885.
16 A. C. Garcia, F. H. B. Lima, E. A. Ticianelli and M. Chatenet, *J. Power Sources*, 2013, **222**, 305–312.
17 X. Yang, S. Li, Y. Liu, X. Wei and Y. Liu, *J. Power Sources*, 2011, **196**, 4992–4995.
18 N. A. M. Harun and N. Shaari, *Int. J. Energy Res.*, 2022, **46**, 17873–17898.
19 I. Merino-Jiménez, C. Ponce de León, A. A. Shah and F. C. Walsh, *J. Power Sources*, 2012, **219**, 339–357.
20 U. B. Demirci, *J. Power Sources*, 2007, **172**, 676–687.
21 M. H. Gouda, W. Gouveia, M. L. Afonso, B. Šljukić, N. A. El Essawy, A. B. A. A. Nassr and D. M. F. Santos, *J. Power Sources*, 2019, **432**, 92–101.
22 N. A. Choudhury, S. K. Prashant, S. Pitchumani, P. Sridhar and A. K. Shukla, *J. Chem. Sci.*, 2009, **121**, 647.
23 Z. Mai, H. Zhang, X. Li, X. Geng and H. Zhang, *Electrochem. Commun.*, 2011, **13**, 1009–1012.

24 C.-C. Huang, Y.-L. Liu, W.-H. Pan, C.-M. Chang, C.-M. Shih, H.-Y. Chu, C.-H. Chien, C.-H. Juan and S. J. Lue, *J. Polym. Sci., Part B: Polym. Phys.*, 2013, **51**, 1779–1789.
25 H. Qin, L. Lin, W. Chu, W. Jiang, Y. He, Q. Shi, Y. Deng, Z. Ji, J. Liu and S. Tao, *J. Power Sources*, 2018, **374**, 113–120.
26 Z. Wang, J. Parrondo, C. He, S. Sankarasubramanian and V. Ramani, *Nat. Energy*, 2019, **4**, 281–289.
27 A. Oshchepkov, A. Bonnefont, G. Maranzana, E. R. Savinova and M. Chatenet, *Curr. Opin. Electrochem.*, 2022, **32**, 100883.
28 P.-Y. Olu, N. Job and M. Chatenet, *J. Power Sources*, 2016, **327**, 235–257.
29 Z. Hu, Q. Xiao, D. Xiao, Z. Wang, F. Gui, Y. Lei, J. Ni, D. Yang, C. Zhang and P. Ming, *ACS Appl. Mater. Interfaces*, 2021, **13**, 53945–53954.
30 Y. Guo, D. Yang, B. Li, D. Yang, P. Ming and C. Zhang, *ACS Appl. Mater. Interfaces*, 2021, **13**, 27119–27128.
31 Z. P. Li, B. H. Liu, J. K. Zhu and S. Suda, *J. Power Sources*, 2006, **163**, 555–559.
32 P.-Y. Olu, F. Deschamps, G. Caldarella, M. Chatenet and N. Job, *J. Power Sources*, 2015, **297**, 492–503.
33 F. G. Boyacı San, O. Okur, Ç. İyigün Karadağ, I. Isik-Gulsac and E. Okumuş, *Energy*, 2014, **71**, 160–169.
34 X. Ren, T. E. Springer, T. A. Zawodzinski and S. Gottesfeld, *J. Electrochem. Soc.*, 2000, **147**, 466–474.
35 X. Geng, H. Zhang, W. Ye, Y. Ma and H. Zhong, *J. Power Sources*, 2008, **185**, 627–632.
36 M. G. Hosseini, R. Mahmoodi and M. S. Amjadi, *Energy*, 2017, **131**, 137–148.
37 Y. Chen, S. Wang and Z. Li, *RSC Adv.*, 2020, **10**, 29119–29127.
38 L. Lin, H. Qin, J. Jia, Z. Ji, H. Chi, H. Ni, J. Wang, Y. He and J. Liu, *J. Alloys Compd.*, 2018, **769**, 136–140.
39 Q. Xiao, M. Cai, M. P. Balogh, M. M. Tessema and Y. Lu, *Nano Res.*, 2012, **5**, 145–151.
40 Y. Yang, Y. Wang, Y. Xiong, X. Huang, L. Shen, R. Huang, H. Wang, J. P. Pastore, S.-H. Yu, L. Xiao, J. D. Brock, L. Zhuang and H. D. Abruña, *J. Am. Chem. Soc.*, 2019, **141**, 1463–1466.
41 G. Rostamikia, R. J. Patel, I. Merino-Jimenez, M. Hickner and M. J. Janik, *J. Phys. Chem. C*, 2017, **121**, 2872–2881.
42 Y. Wang, Y. Yang, S. Jia, X. Wang, K. Lyu, Y. Peng, H. Zheng, X. Wei, H. Ren, L. Xiao, J. Wang, D. A. Muller, H. D. Abruña, B. J. Hwang, J. Lu and L. Zhuang, *Nat. Commun.*, 2019, **10**, 1506.
43 H. Cheng and K. Scott, *J. Power Sources*, 2006, **160**, 407–412.
44 F. G. Boyacı San, Ç. İyigün Karadağ, O. Okur and E. Okumuş, *Energy*, 2016, **114**, 214–224.
45 D. R. Baker, D. A. Caulk, K. C. Neyerlin and M. W. Murphy, *J. Electrochem. Soc.*, 2009, **156**, B991.
46 J. Wang, *Energy*, 2015, **80**, 509–521.
47 L. Qi, Z. Zheng, C. Xing, Z. Wang, X. Luan, Y. Xue, F. He and Y. Li, *Adv. Funct. Mater.*, 2022, **32**, 2107179.
48 J. Chang, G. Wang, W. Zhang and Y. Yang, *J. Energy Chem.*, 2022, **68**, 439–453.
49 J. Fan, M. Chen, Z. Zhao, Z. Zhang, S. Ye, S. Xu, H. Wang and H. Li, *Nat. Energy*, 2021, **6**, 475–486.
50 S. W. Linehan, A. A. Chin, N. T. Allen, R. Butterick, N. T. Kendall, I. L. Klawiter, F. J. Lipiecki, D. M. Millar, D. C. Molzahn and S. J. November, *Low-Cost Precursors to Novel Hydrogen Storage Materials*, Rohm and Haas Company, Philadelphia, PA, 2010.
51 D. A. Werner, C. C. Huang and D. Aminoff, *Anal. Biochem.*, 1973, **54**, 554–560.
52 G. Kresse and J. Hafner, *Phys. Rev. B:Condens. Matter Mater. Phys.*, 1993, **47**, 558–561.
53 P. E. Blöchl, *Phys. Rev. B:Condens. Matter Mater. Phys.*, 1994, **50**, 17953–17979.
54 G. Kresse and J. Furthmüller, *Phys. Rev. B:Condens. Matter Mater. Phys.*, 1996, **54**, 11169–11186.
55 J. P. Perdew, J. A. Chevary, S. H. Vosko, K. A. Jackson, M. R. Pederson, D. J. Singh and C. Fiolhais, *Phys. Rev. B:Condens. Matter Mater. Phys.*, 1992, **46**, 6671–6687.
56 V. I. Anisimov, J. Zaanen and O. K. Andersen, *Phys. Rev. B:Condens. Matter Mater. Phys.*, 1991, **44**, 943–954.
57 F. Zhou, M. Cococcioni, C. A. Marianetti, D. Morgan and G. Ceder, *Phys. Rev. B:Condens. Matter Mater. Phys.*, 2004, **70**, 235121.
58 A. Rushiti, C. Hättig, B. Wen and A. Selloni, *J. Phys. Chem. C*, 2021, **125**, 9774–9781.
59 J. K. Nørskov, J. Rossmeisl, A. Logadottir, L. Lindqvist, J. R. Kitchin, T. Bligaard and H. Jónsson, *J. Phys. Chem. B*, 2004, **108**, 17886–17892.